In Situ Techniques for Quinone-Mediated Electrochemical Carbon Capture and Release in Aqueous Environments

Kiana Amini[1], Thomas Cochard[1], Yan Jing[2], Jordan D. Sosa[1], Dawei Xi[1], Maia Alberts[1], Michael S. Emanuel[1], Emily F. Kerr[2], Roy G. Gordon[2], Michael J. Aziz[1]✉

1. John A. Paulson School of Engineering and Applied Sciences, Harvard University, Cambridge, Massachusetts 02138, United States

2. Department of Chemistry and Chemical Biology, Harvard University, Cambridge, Massachusetts 02138, United States

✉ E-mail: maziz@harvard.edu

Abstract

We present two novel experimental techniques designed to quantify the contributions of nucleophilicity-swing and pH-swing mechanisms to carbon capture in the electrochemical aqueous quinone-based CO_2 capture process. Through thermodynamic analysis, we elucidate the intricate interplay between these two mechanisms, and emphasize the critical role of understanding this interplay in the material discovery cycle for carbon capture applications. This insight prompts the development of two innovative *in situ* techniques. The first technique capitalizes on discernible voltage signature differences between quinone, and quinone-CO_2 adducts. By incorporating a reference electrode into the carbon capture cell setup, we apply this method to investigate bis[3-(trimethylammonio)propyl]-anthraquinones (BTMAPAQs). Our findings reveal the isolated contributions of nucleophilicity-swing and pH-swing mechanisms to overall carbon capture capacity under varying wait times and CO_2 partial pressures. The second method is developed based on our finding that the adduct form of the quinone exhibits a fluorescence emission from an incident light at wavelengths distinct from the fluorescence of the reduced form, enabling differentiation through optical band-pass filtering at each unique fluorescent signature. Thus, we introduce a non-invasive, *in situ* approach using fluorescence microscopy, providing the unique capability to distinguish between oxidized, reduced, and adduct species with sub-second time resolution at single digit micrometer resolution. This powerful technique holds significant promise for studying such systems, representing an advancement in our ability to understand carbon capture processes.

Introduction

The quest for clean energy has become increasingly important in today's world, driven by the urgent need to address climate change and reduce greenhouse gas emissions. While the advancement of energy storage technologies and the broader adoption of renewable energy sources is vital for transitioning to a cleaner energy future [1], a parallel focus on carbon capture technologies is equally important. Effective carbon management is vital for addressing emissions from some of the toughest-to-abate sectors, such as heavy industries like steel production and cement manufacturing. These industries face challenges in rapidly reducing their reliance on fossil fuels. Therefore, parallel efforts to advance carbon capture technologies are essential and play a crucial role in mitigating these sectors' environmental impact during the transition and beyond [2].

The conventional approach to capturing CO_2 from dilute sources involves amine scrubbing technology, where CO_2 is captured at 40°C and released at 120°C [3]. However, these thermochemical techniques pose challenges due to their energy-intensive nature, driven by operation at elevated temperatures. Additionally, they are susceptible to issues such as thermal degradation and corrosion of equipment, as well as the emission of volatile amines [4]. In pursuit of more efficient alternatives, researchers have directed their

focus towards the development of electrochemical technologies for this purpose. Electrochemical systems offer the advantage of isothermal operation, relying on an electrical gradient to drive a redox reaction that can directly or indirectly create an affinity in the system for CO_2 capture [5-9].

One of the promising electrochemical carbon capture systems relies on quinone chemistry. Quinones are organic molecules containing an unsaturated six-member ring with two carbonyl groups. They exhibit two potential mechanisms of CO_2 capture. Firstly, the nucleophilicity-swing mechanism occurs in aprotic solvents during electrochemical redox reactions. The phenolate groups upon quinone reduction reversibly react with carbon dioxide via nucleophilic addition, which results in the formation of quinone-CO_2 adducts. Secondly, the pH-swing mechanism occurs in protic solvents. Depending on the pK_a of the hydroquinones and the local pH, the electrochemical reduction of quinones can be proton-coupled and creating hydroxide ions, which capture CO_2 as carbonate or bicarbonate. The majority of the quinones reported in literature for CO_2 capture applications have been dissolved in aprotic solvents [10-12] or immobilized on the electrodes [6,10,13,14], demonstrating a nucleophilicity-swing mechanism. One exception is our recent report on the first aqueous quinone flow chemistry-enabled electrochemical CO_2 capture process, which was based on bis[3-(trimethylammonio)propyl]-anthraquinones (BTMAPAQs) [15]. Such aqueous systems are highly attractive due to the safety and cost-effectiveness they offer by utilizing water, which is non-flammable and cheap. Additionally, aqueous electrolytes feature high ionic conductivity. This prior work demonstrated that, given the aqueous nature of the system, both pH-swing and nucleophilicity-swing mechanisms contribute to CO_2 capture across a range of operational conditions. However, traditional methods of measuring the total amount of CO_2 captured or released only allow for reporting the combined contribution of these two mechanisms.

In this study, we address the imperative need to quantify the contributions of the nucleophilicity-swing and pH-swing mechanisms. The first two sections lay the foundation for this exploration. Firstly, we provide a thermodynamic overview elucidating the interplay between these mechanisms, emphasizing how the dominance of one over the other necessitates specific molecular engineering considerations in the material discovery cycle. Secondly, we delve into a case study focusing on BTMAPAQ, extracting both thermodynamic and kinetic insights for its three isomers. This case study highlights that, beyond thermodynamics, the kinetics of these mechanisms can differ, thereby influencing the dynamic interplay between them. Building on these foundational sections, we introduce two *in situ* experimental methods for quantifying the contributions of these mechanisms in the system. The first method relies on discerning the voltage signature differences between the quinone and the quinone-CO_2 adduct. The second method introduces a powerful non-invasive, *in situ* method based on fluorescence microscopy, offering the capability to distinguish between the oxidized, reduced, and adduct species and quantify their concentration with sub-second time resolution at single digit micrometer resolution through their fluorescence signatures, demonstrating a highly promising technique for studying such electrochemical systems.

Thermodynamic Overview

To demonstrate the influence of various properties of the hypothetical anthraquinone molecule employed in the system on the interplay between nucleophilicity-swing and pH-swing mechanisms, we analyze a set of equations inherent to the system. The fully reduced anthraquinone (AQ^{2-}) molecule in an aqueous solution can either undergo the direct capture of CO_2 through $AQ(CO_2)_2{}^{2-}$ adduct formation or engage in a proton-coupled reaction:

$$AQ^{2-} + 2CO_2(aq) \leftrightarrow AQ(CO_2)_2{}^{2-} \quad K_{AQ\_adduct} = \frac{[AQ(CO_2)^{2-}]}{[AQ^{2-}]*[CO_2(aq)]^2} \quad (1)$$

$$AQ^{2-} + 2H^+ \leftrightarrow AQH_2 \quad K_{protonation} = \frac{[AQH_2]}{[AQ^{2-}]*[H^+]^2} \quad (2)$$

where the K_{AQ_adduct} and $K_{protonation}$ are the $AQ(CO_2)_2{}^{2-}$ adduct formation and protonation equilibrium constants, respectively. Both reactions can occur in two steps, involving the sequential acceptance of the first CO_2 or H^+ molecule followed by the second. The experimental determination of K_{AQ_adduct} is elucidated in the next section through cyclic voltammetry, although extracting the equilibrium constant for the initial step in isolation presents challenges. Conversely, the double step protonation can be deduced from the Pourbaix diagram, from the pKa_1 and pKa_2 of the compound, resulting in the following equilibrium equations:

$$AQH^- + H^+ \leftrightarrow AQH_2 \quad K_1 = \frac{[AQH_2]}{[AQH^-]*[H^+]} \quad (3)$$

$$AQ^{2-} + H^+ \leftrightarrow AQH^- \; K_2 = \frac{[AQH^-]}{[AQ^{2-}]*[H^+]} \quad (4)$$

Reactions 3 and 4 result in the consumption of protons and an increase in the pH of the solution. The produced hydroxides can then undergo bicarbonate and carbonate formation reactions, resulting in an indirect capture of CO_2:

$$CO_2(aq) + H_2O \leftrightarrow HCO_3^- + H^+ \quad K_4 = \frac{[HCO_3^-]*[H^+]}{[CO_2(aq)]} \quad (5)$$

$$HCO_3^- \leftrightarrow CO_3^{2-} + H^+ \quad K_5 = \frac{[CO_3^{2-}]*[H^+]}{[HCO_3^-]} \quad (6)$$

Reactions (1) – (6) involve the consumption or production of various charge species. In the solution, charge neutrality must always be maintained. Thus,

$$+ 2[AQ^{2-}] + 2\left[AQ(CO_2)_2{}^{2-}\right] + [AQH^-] + [OH^-] + [HCO_3^-] + 2[CO_3^{2-}] - [H^+] - [M^+] = 0 \quad (7)$$

where M^+ represents the counterion resulting from dissolving the anthraquinone salt in the solution (e.g., K^+, Na^+). Additionally, the sum of concentrations of all AQ-containing molecules is conserved at its total dissolved concentration (C_T). Therefore,

$$+ [AQ^{2-}] + \left[AQ(CO_2)_2{}^{2-}\right] + [AQH^-] + [AQH_2] - (C_T) = 0 \quad (8)$$

An additional constraint arises from the water dissociation equilibrium resulting in:

$$H_2O \leftrightarrow OH^- + H^+ \quad K_w = [OH^-][H^+] \quad (9)$$

Finally, the concentration of the $CO_2(aq)$ is dictated by the partial pressure of CO_2 (pCO_2) and follows Henry's Law:

$$[CO_2(aq)] = C_{Henry} pCO_2 \quad (10)$$

where C_{Henry} is the Henry's constant, assumed to be 35 mM/bar at room temperature. Given that the present thermodynamic analysis serves as an overview of the interplay between the nucleophilicity-swing and pH-swing mechanisms, we focus on the above main reactions while those leading to intermediate compounds such as $AQ(CO_2)^{2-}$ and $AQHCO_2^-$ and species formed due to mixed mechanisms are assumed to be disregarded for lack of estimation for them and for simplicity.

Here, we begin by considering a total concentration of 0.1 M AQ dissolved under a partial pressure of 0.1 bar. With pKa_1 and pKa_2 set at 11 and 13, respectively—values typical for several anthrahydroquinones reported to date [15-18]—we further consider equilibrium constants K_4, K_5, and K_w as $1.1 * 10^{-6}\ M$ [19], $4.1 * 10^{-10}\ M$ [19], and $10^{-14}\ M^2$, respectively. Regarding the equilibrium constants for bicarbonate and carbonate formation, we assume that the presence of 0.1 M AQ has not significantly altered the salinity of the solution and the numbers are taken at salinity of zero. Under these specified conditions, Figure 1 illustrates the dynamic interplay between nucleophilicity-swing and pH-swing mechanisms in the capture of CO_2, as a function of the $AQ(CO_2)_2^{2-}$ adduct formation equilibrium constant. This analysis predicts that at K_{AQ_adduct} less than $10^{12}\ M^{-2}$, the thermodynamic driving force for nucleophilicity-swing mechanism is too low and thus the CO_2 capture proceeds mainly via pH-swing mechanism. The opposite is correct for K_{AQ_adduct} values above $10^{17}\ M^{-2}$. Between these two limits, both mechanisms contribute to the capture of CO_2. Understanding this interplay in relation to the properties of the employed molecule is crucial in the context of the material discovery cycle for carbon capture applications. For instance, if a newly synthesized molecule, under the desired operational conditions, exhibits primarily the pH-swing capture mechanism, optimizing the molecule's capture capacity necessitates a focus on maximizing its pKa, as well as solubility, to increase the concentration of OH^- molecules produced. Conversely, for molecules with strong adduct formation equilibrium constants, maximizing pKa becomes irrelevant, and attention should be directed merely toward enhancing the solubility of the AQ molecule. These considerations are illustrated in Figures 1b-c and S1. For intermediate values of K_{AQ_adduct} (e.g., $10^{14}\ M^{-2}$), where both mechanisms are at play, increasing the pKa of the AQ molecule shifts the contribution more towards bicarbonate/carbonate formation, as depicted in Figure 1b. In contrast, under conditions where K_{AQ_adduct} is strong (e.g., $10^{22}\ M^{-2}$), even with limited pKa values (e.g., $pKa_1 = 7$ and $pKa_2 = 7$), the $AQ(CO_2)_2^{2-}$ adduct formation mechanism captures up to the expected capacity independent of enhancements in pKa_2 (see Figure S1a). However, under such limiting conditions, when K_{AQ_adduct} is weak (e.g., $10^4\ M^{-2}$), increasing the pKa of anthrahydroquinone molecule becomes a crucial factor for enhancing the capture capacity as depicted in Figure S1a.

Another important factor is the effect of CO_2 partial pressure. Under the conditions set in Figure 1a and for intermediate values of K_{AQ_adduct} (e.g., $10^{14}\ M^{-2}$), where both mechanisms are at play, increasing pCO_2 to values higher than 0.1 bar, would indeed increase the $CO_2(aq)$ concentration according to the Henry's law, but it results in negligible change in the individual contribution of nucleophilicity-swing and pH-swing mechanisms toward the total capture, as shown in Figure 1c and 1d. However, at dilute CO_2 concentrations (less than 0.05 bar), the thermodynamic driving force for $AQ(CO_2)_2^{2-}$ adduct formation drops and in the bicarbonate/carbonate equilibration, carbonate formation contribution increases, which would have effect on the capacity of the capture. In the adduct formation pathway, each AQ molecule captures two CO_2 molecules by engaging both nucleophilic oxygen sites. Meanwhile, in the pH-swing pathway, a two-step protonation process yields two OH^- ions per AQ molecule. When these hydroxides predominantly form bicarbonate groups, each OH^- captures one CO_2, resulting in a 2 CO_2 capture capacity per one AQ molecule. Contrastingly, carbonate formation consumes two OH^- ions, resulting in a 1 CO_2 capture capacity per one AQ molecule. Therefore, $AQ(CO_2)_2^{2-}$ adduct formation and bicarbonate formation both exhibit a capture capacity ratio of 2 to 1, while carbonate formation yields a 1 to 1 ratio. In the context of the interplay between nucleophilicity-swing and pH-swing mechanisms, one can see that for the molecules where K_{AQ_adduct} is strong (e.g., $10^{22}\ M^{-2}$), the thermodynamic driving force for $AQ(CO_2)_2^{2-}$ adduct formation is very strong, and even at dilute CO_2 concentrations (400 ppm), the capture

capacity proceeds at a 2-1 ratio through nucleophilicity-swing mechanisms (see Figure S1b). Conversely, when K_{AQ_adduct} is weak (e.g., $10^4\ M^{-2}$), the dominant mechanism becomes pH-swing, and reducing pCO_2 to values less than 0.05 bar shifts the equilibrium towards carbonate formation, diminishing the capture capacity to a 1 to 1 ratio.

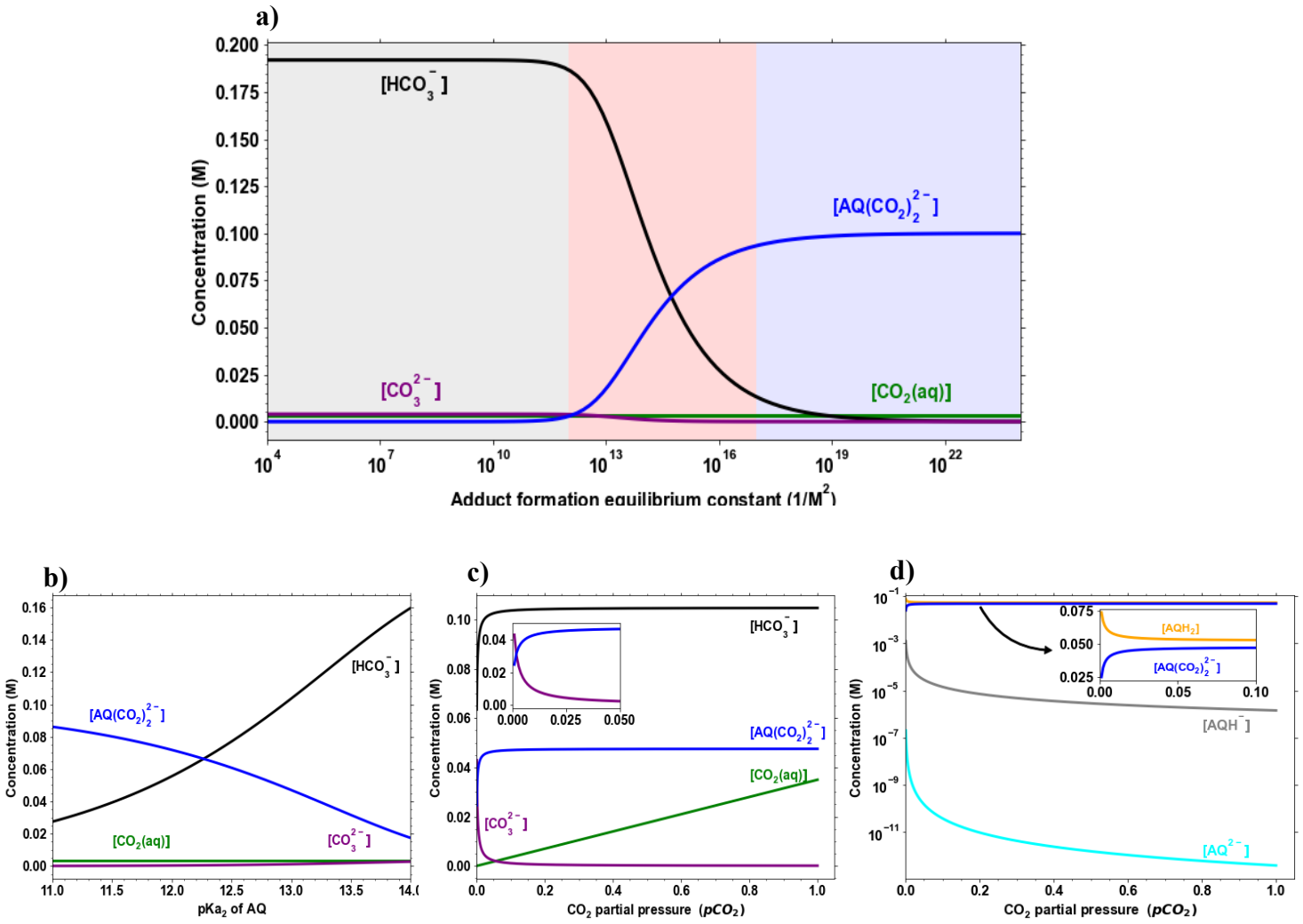

Figure 1 *Equilibrium concentrations determined by solving the corresponding equilibrium equations described in this section. Unless specified, a total concentration of 0.1 M AQ dissolved under a partial pressure of 0.1 bar is assumed. The AQ pKa_1 and pKa_2 values are set at 11 and 13, respectively, with equilibrium constants K_4, K_5, and K_w at $1.1 * 10^{-6}\ M$, $4.1 * 10^{-10}\ M$, and $10^{-14}\ M^2$, respectively, and K_{AQ_adduct} of $10^{14}\ M^{-2}$. a) Concentration profiles of HCO_3^-, CO_3^{2-}, $CO_2(aq)$, $AQ(CO_2)_2{}^{2-}$ at different K_{AQ_adduct} values ($AQ(CO_2)_2{}^{2-}$ adduct formation equilibrium constants). b) Concentrations of HCO_3^-, CO_3^{2-}, $CO_2(aq)$, $AQ(CO_2)_2{}^{2-}$ at varying pKa_2 values of the AQ molecule. c) Concentrations of HCO_3^-, CO_3^{2-}, $CO_2(aq)$, $AQ(CO_2)_2{}^{2-}$ at different partial pressures of CO_2. d) Concentrations of AQ^{2-}, $AQ(CO_2)_2{}^{2-}$, AQ, AQH^- at different partial pressures of CO_2.*

Thermodynamic and Kinetic Analysis of BTMAPAQ Isomers

In this section, we present a case study for the specific case of BTMAPAQ isomers. These molecules are utilized in the first aqueous quinone flow electrochemical CO_2 capture process [15].

Figure 2 illustrates the cyclic voltammetry of 1,4-, 1,5-, and 1,8-BTMAPAQ isomers at various scan rates under a pure stream of CO_2. For comparison, the cyclic voltammetry of these compounds under a pure stream of N_2 is depicted as a dashed line at 300 mV/s. The CV plots of the isomers at all other scan rates under a pure N_2 headspace is further shown in Figure S2. For each isomer, a new oxidation peak emerges under the CO_2 headspace, shifted to more positive potentials compared to that under pure N_2 headspace, while the reduction peak remains almost identical. The more positive oxidation peak corresponds to the newly formed $AQ(CO_2)_2^{2-}$ redox-active species, which cannot exist under the pure nitrogen environment. The less positive redox potential is attributed to the AQ^{2-} oxidation given that it is occurring under the nitrogen headspace. The observation that the nucleophilicity-swing mechanism leads to the formation of a new redox-active species with a distinct redox potential signature compared to the original AQ molecule enables us to utilize these CVs for extracting information regarding the nucleophilicity-swing mechanism. In the thermodynamic context, the equilibrium constants for $AQ(CO_2)_2^{2-}$ adduct formation for these isomers can be deduced by examining the difference in the oxidation peaks associated with the AQ^{2-} and $AQ(CO_2)_2^{2-}$ redox reactions [20]. The K_{AQ_adduct} can be calculated with the following equation (derivation included in SI Section 2.2 and Figure S3):

$$K_{AQ\_adduct} = \exp\left(\frac{nF}{RT}\left(E^{0\prime}_{AQ_{adduct}} - E^{0\prime}\right)\right) \quad (11)$$

where n is the number of transferred electrons, F is the Faraday's constant, R is the gas constant, T is the temperature and $E^{0\prime}_{AQ\_adduct}$ and E'^0 are the half-wave redox potential for the $AQ(CO_2)_2^{2-}$ adduct redox reaction and the AQ^{2-} redox reaction, respectively, as elucidated in the SI Section 2.2. Using equation (11), we find the K_{AQ_adduct} to be $1.6 * 10^{22}$, $7.3 * 10^{21}$ and $2.8 * 10^{18}$ M^{-2} for the isomers 1,4-, 1-5, and 1-8-BTMAPAQ, respectively. Comparing with the predictions from the equilibrium model shown in Figure 1a, these are attributed to a very strong $AQ(CO_2)_2^{2-}$ adduct formation region, predicting a system dominated by nucleophilicity-swing mechanism.

While thermodynamics provides valuable insights, it is crucial to recognize that kinetics constitutes another integral aspect of the overall process. A mechanism may exhibit thermodynamic favorability, yet it can be kinetically too slow to occur. In order to gain some understanding of the kinetics of the reaction, we conducted the CV tests under different scan rates as shown in Figure 2. At higher scan rates, the CV is swept faster across the same potential range, resulting in a quicker run. Given that under CO_2, a chemical reaction is occurring ($AQ(CO_2)_2^{2-}$ adduct formation, according to reaction (1)), there would be less time for the chemical reaction to proceed at higher scan rates. It can be observed that for the 1,4- and 1,5-BTMAPAQ isomers, increasing the scan rate would barely result in any current being extracted at the oxidation potential attributed to the oxidation of AQ^{2-}, which implies that the chemical quinone-adduct formation reaction is occurring at rates faster than the scan rates used. Thus, even at 1000 mV/s, we extract current predominantly from $AQ(CO_2)_2^{2-}$. Interestingly, for the 1,8-BTMAPAQ isomer, increasing the scan rate reveals a growing peak at the oxidation potentials related to AQ^{2-} oxidation, which indicates that

the chemical reaction rate of $AQ(CO_2)_2^{2-}$ adduct formation is slower for this isomer compared to the other two isomers and cannot keep up with the fast rate of potential change. In order to quantify the kinetic rates associated with the $AQ(CO_2)_2^{2-}$ adduct formation reaction, we assume the following three-step electrochemical-chemical-electrochemical (ECE) reaction scheme:

- $AQ + 2\ e^- \leftrightarrow AQ^{2-}$ $E_1^{o\prime}, k_0$ (12)
- $AQ^{2-} + 2\ CO_2 \rightarrow AQ(CO_2)_2^{2-}$ k_c (13)
- $AQ(CO_2)_2^{2-} \rightarrow AQ + 2\ CO_2 + 2\ e^-$ $E_2^{o\prime}, k_0'$ (14)

The reversible AQ redox reaction occurs at $E_1^{o\prime}$ formal potential with an electrochemical rate constant of k_0. The chemical quinone-adduct formation reaction occurs at a chemical rate constant of k_c, which would result in $AQ(CO_2)_2^{2-}$ species with a redox reaction occurring at $E_2^{o\prime}$ formal potential and with k'_0 electrochemical rate constant. It is important to note that the AQ redox reaction (reaction (12)) unfolds in two single electron steps, as detailed in the SI Section 2.3. However, these two steps occur with less than 30 mV separation (see Section 2.3 and Figure S4), leading to a single merged peak in the cyclic voltammogram profile, and thus, the assumption is made that reaction (12) proceeds in one two-electron step. Similarly, reaction (14) may occur in two sequential steps but based on the shape of the merged peaks in the CV profile, these sequential steps must occur with small potential separations. The nearly identical location of the reduction peak under both N_2 and CO_2 environments suggests that the sequential reduction of AQ is unaffected by CO_2 complexation. Considering these observations, we proceeded with fitting the CV profiles to the ECE scheme, with details provided in SI Section 2.4. Examples of a fitting for 1,8-BTMAPAQ are shown in Figure 2d, and the rest of the fittings are provided in Figures S5-S7, indicating a very good agreement between the model and the experimental data. It is important to note that the properties of the AQ redox reaction (reaction (12)), such as its electrochemical reaction rate constant and diffusion coefficient can be extracted in isolation under nitrogen environment. Figures S9-S11 show the properties extracted from rotating disk electrode tests under a nitrogen environment for all the isomers. The fitting parameters achieved for AQ under CO_2 are close to the range of the extracted properties of AQ in isolation under a nitrogen environment. For 1,4- and 1,5-BTMAPAQ isomers, an increase in scan rate barely results in current extraction at the potential relevant to AQ reduction. Therefore, we report a lower limit on k_c for these two isomers, below which the chemical reaction would be too slow to keep up with the fast scan rates. However, for 1,8-BTMAPAQ, an exact value of k_c, rather than a limit, is reported.

The extracted parameters for the three isomers are presented in Table 1. The k_c values are >6.7, >6.0, 2.4 s^{-1} which would be >192, >171, and 68.6 $M^{-1}s^{-1}$ (per moles of CO_2) for 1,4-, 1,5-, and 1,8-BTMAPAQ isomers, respectively, indicating the rate constant for the occurrence of the nucleophilicity-swing mechanism. In contrast, the rate constant for bicarbonate/carbonate formation that is occurring in the pH-swing mechanism is reported to be $12.1 * 10^3\ M^{-1}s^{-1}$ at 25°C [21], significantly higher than what we are reporting for the $BTMAPAQ(CO_2)_2^{2-}$ adduct formation mechanism. Having obtained the rate constants, we can predict the rates of both bicarbonate formation and the formation of the $BTMAPAQ(CO_2)_2^{2-}$ adduct under various conditions (SI Section 2.5), which demonstrates the extent to which bicarbonate formation can proceed more rapidly than the $BTMAPAQ(CO_2)_2^{2-}$ adduct formation under different conditions. Note that the protonation reaction of AQ needs to occur first before the bicarbonate/carbonate reaction can proceed. Therefore, the rate of protonation is also crucial. However, given the reports on the concerted protonation of quinones with the electron transfer in aqueous media [22], it is reasonable to

assume that the rate of the bicarbonate/carbonate reactions is the limiting factor in the pH-swing mechanism. This comparison highlights that although thermodynamically we predict the adduct formation mechanism to occur predominantly for these three isomers, kinetically the pH-swing mechanism is more favorable.

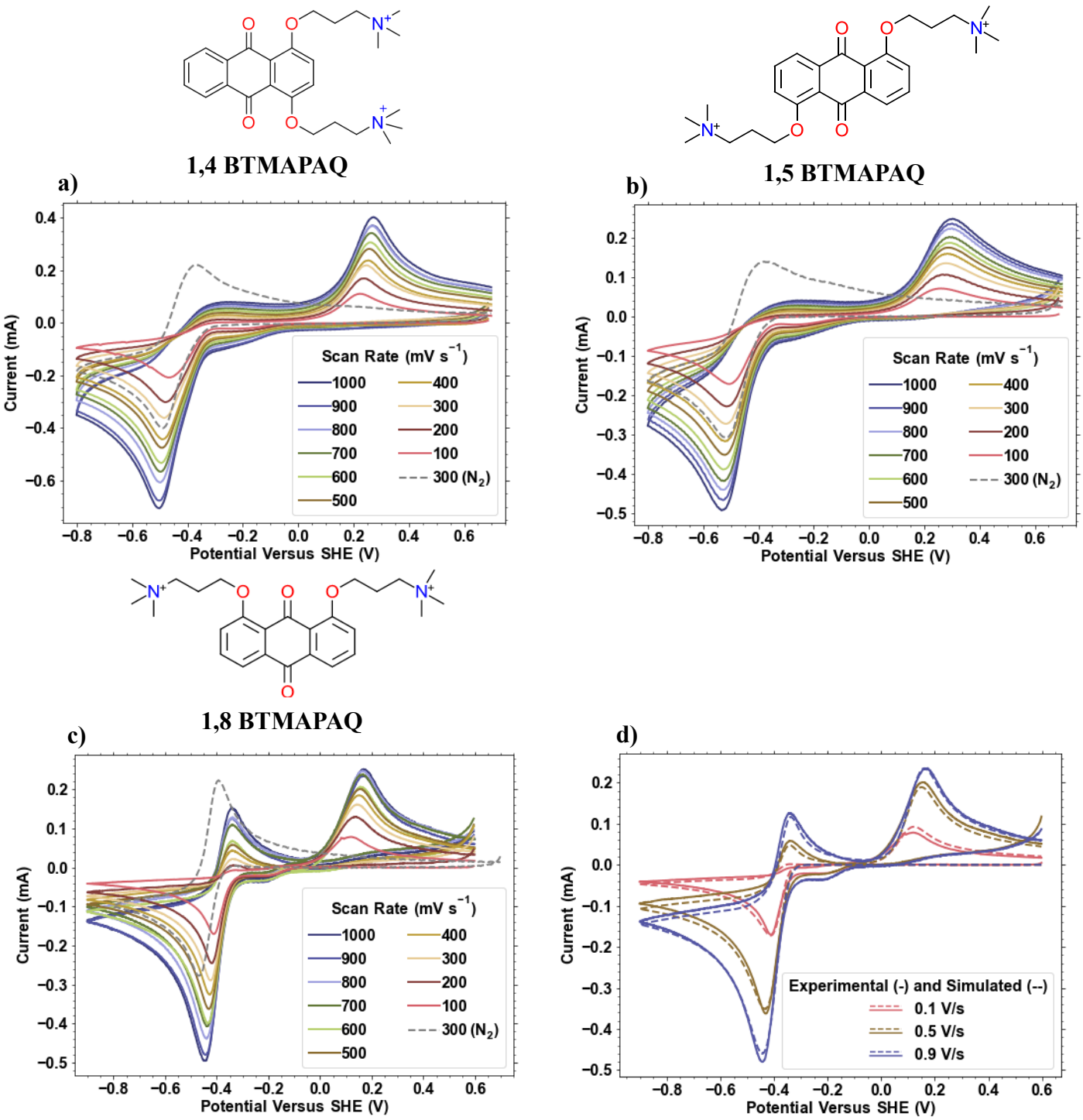

Figure 2 *Molecular Structures and cyclic voltammetry profiles of 5 mM of a) 1,4-BTMAPAQ, b) 1,5-BTMAPAQ* and c) *1,8-BTMAPAQ dissolved in 1 M KCl under a pure CO_2 headspace at different scan rates between 100 mV/s to 1000 mV/s. For comparison, the cyclic voltammetry profile under a pure N_2 headspace is also depicted as a dashed line at a scan rate of 300 mV/s for each isomer. d) The experimental and fitted cyclic voltammetry profiles of 1,8-BTMAPAQ for three scan rates of 0.1 V/s, 0.5 V/s, and 0.9V/s.*

Table 1: *Parameters extracted from fitting experimental cyclic voltammetry profiles of BTMAPAQ isomers to the ECE mechanism scheme.*

Parameters	1-4BTMAPAQ	1-5BTMAPAQ	1-8BTMAPAQ
k_0 [cm/s]	1.46E-3	5.11E-4	1.75E-3
k_0' [cm/s]	4.90E-4	1.14E-3	6.70E-3
k_c [1/ s]	6.7	6.0	2.4
E_1^o [V vs Ag/AgCl]	-0.470	-0.451	-0.478
E_2^o[V vs Ag/AgCl]	0.007	0.107	0.034
α_1	0.32	0.23	0.37
α_2	0.54	0.66	0.64
D [cm^2/s]	3.29E-6	1.00E-6	1.00E-6
D_{add} [cm^2/s]	5.69E-6	2.34E-6	2.02E-6

In Situ Methods for Investigation of Nucleophilicity-Swing and pH-Swing Mechanisms in Aqueous Media

The previous two sections underscore the necessity for an experimental methodology capable of discerning the intricate interplay between the pH-swing and nucleophilicity-swing mechanisms. The dominance of either mechanism determines the specific properties of the AQ molecule that warrant attention for enhancing carbon capture capacity. Furthermore, predictions based on thermodynamics and kinetics are contingent upon certain assumptions that may be challenged at the system level. Additionally, predictions based on thermodynamics and kinetics may draw opposing conclusions regarding the dominance of one mechanism over the other. Consequently, the need for an experimental technique to differentiate between these mechanisms becomes essential. As shown in Figure S12, using pH as an indicator for the amount of OH^- formed during the reaction is insufficient, primarily due to the buffering effect of the carbonate/bicarbonate system. In the following sections, we introduce two new *in situ* experimental techniques designed for this purpose.

In Situ Method 1: Reference Electrodes

The cyclic voltammetry plots depicted in Figure 2 reveal the distinct oxidation potential signature of the BTMAPAQ$(CO_2)_2^{2-}$ adduct in comparison to the reduced BTMAPAQ molecules. This discernible voltage separation should allow us to accurately quantify the contribution of nucleophilicity-swing toward total carbon capture. To illustrate this method and investigate its sensitivity, we conducted experiments utilizing

a flow cell comprising 12 ml of 0.1 M 1,5BTMAPAQ paired with 40 ml of 0.2 M BTMAPFC. Figure 3a presents the measured parameters—voltage, pH, upstream gas ratio, measured partial pressure of CO_2, and flow rate at the downstream—during this experiment. While the CO_2 sensor and flowmeter provide the total amount of capture and release, they are unable to differentiate the specific mechanism contributing to the overall capture. Hence, in the electrolyte path to the battery, we introduced a reference electrode to measure the real-time potential of the negative electrode against the reference electrode. Utilizing this setup, the cell was intentionally charged in a nitrogen environment, followed by a controlled purge with 0.1 bar CO_2 and 0.9 bar of N_2 for varying durations (60 minutes in Figure 3a), followed by a switch back to the nitrogen environment. This experimental procedure with different purge durations (15, 30, and 60 minutes) was intentionally designed to allow us to control the amount of adduct formation during the course of the experiment and examine its relationship with the discharge voltage profiles.

The voltage profile depicted in Figure 3a is zoomed in the upper plot of Figure 3b, accompanied by its corresponding negative half-cell potential measured from the reference electrode. Two distinct plateaus emerge in the full cell voltage profile, mirroring the double plateaus identified in the negative half-cell potential plot. The more negative discharge potential, averaged at -0.3 V vs SHE, aligns well with the oxidation potential of the reduced species from the cyclic voltammetry profiles, while the less negative half-cell potential at 0.1 V vs SHE is close to the adduct species' potential signature. We attribute the differences between the cell potential and the CV potentials to the possible local pH and electrolyte composition differences. Given this distinctive potential separation, we can calculate the adduct formation by examining the capacity delivered at the voltage signature of the quinone-adduct compound. As depicted in Figure 3c, extending the duration of CO_2 purging from 15 minutes to 60 minutes clearly shows an increase in the capacity delivered at the potential signature of the adduct species. In separate experiments, we purged with 0.1 bar CO_2 and 0.9 bar of N_2 from the beginning of the experiment with a 120-minute purging during the rest-time, clearly demonstrating that such a prolonged purging duration would increase the capacity delivered by the adduct. Eventually, in the case of 7 hours of purging, the entire discharge capacity is exclusively delivered by the adduct species.

Figure 3d (top) illustrates the CO_2 release volume calculated both from sensor measurements and the oxidation voltage signature of the adduct for experiments done in Figure 3a and 3b (see Figure S13). The volume obtained from the sensor includes the combined contribution of nucleophilicity-swing and pH-swing mechanisms, while the CO_2 volume determined by deducing the adduct concentration from the half-cell discharge voltages represents solely the contribution of the adduct. As a result, the disparity between these two values is attributed to the pH-swing mechanism. In Figure 3d, we've also presented the maximum theoretical CO_2 that can be anticipated from this system based on the total discharge capacity. The total theoretical CO_2 capacity, based on discharge capacities, is within the same range across all the experiments. This consistency is observed given that, in all tests, 12 ml of 0.1 M 1,5-BTMAP AQ was prepared. Furthermore, as anticipated, an increase in the duration of the CO_2 purge time leads to a proportional rise in the total captured amount measured by the sensor. Interestingly, the contribution of the pH-swing mechanism versus the nucleophilicity-swing mechanism changes across these experiments. In Figure 3d (bottom), the percentage contribution of each mechanism to the total capture amount is presented. For the short 15-minute duration tests, we observe a 40% contribution from the pH-swing mechanism. However, with a prolonged 7-hour purge time, the capture predominantly occurs through the nucleophilicity mechanism. This observation aligns very well with our earlier discussions on the thermodynamic and kinetic predictions for the BTMAPAQ isomers, demonstrating slow kinetics of nucleophilicity-swing mechanism compared to the pH-swing mechanism but eventual equilibrium domination of the

nucleophilicity-swing mechanism. Subsequently, our attention turned to conducting tests at high concentrations of 0.4 M and very diluted CO_2 concentrations of 0.01 (1% CO2, 99% N2) (See Figure S14). At these high AQ concentrations, the salinity of the solution deviates from the assumptions made in our modeling scheme. Furthermore, owing to the extremely low concentrations of CO_2, extended purge durations are necessary to achieve high capture capacities. Figure 3e illustrates the measurements conducted over different durations of purge time (1 – 10 hours). In these experiments at high concentration of BTMAPAQ, we observe the dominance of the nucleophilicity-swing mechanism in all tests. Experiments shown in Figure 3 suggests a potential exchange reaction between the organic carbonate adduct and inorganic carbonate, drawing parallels to the reported self-exchange electron-transfer reactions observed between diamagnetic and paramagnetic ions of anthraquinones [23]. In the present paper, our primary focus is on introducing *in situ* methods for quantification of these phenomena. However, the observed potential exchange reaction between the organic carbonate adducts and inorganic carbonate is intriguing and warrants further investigation.

Note that in this electrolyte, effectively a mixture of two redox-active species (reduced and the adduct) has formed. As per our prior work on mixed organic redox-active species [24], when the potential separation between two mixed species is over 300 mV, the concentration of the first redox species is consumed before the second redox event begins. This means that for the present case, the capacity at each plateau can be directly correlated with the corresponding species concentration. If the potential separations were less than 300 mV, it is expected to have a certain degree of oxidation of the adduct from the start of the discharge phase. In such a case, a modeling scheme such as the one developed in our prior work [24] must be used for the accurate prediction of the concentrations.

These tests illustrate that leveraging the voltage signature difference of the quinone-adduct compound provides a viable method for gaining insights into the contribution of the nucleophilicity mechanism. However, it's crucial to note that while the capture process takes place either at the onset of CO_2 purge during the charging phase or during the rest time after charging, we cannot quantify the concentration of the quinone-adduct species until the discharge occurs and we examine the discharge voltage profiles. In simpler terms, although this method is conducted *in situ*, meaning measurements are taken during the test, it is essentially an 'aftermath' method, as the quantification of the quinone-adduct occurs post-capture. In the next section, we introduce a method for real-time measurement of the adduct during the capture phase.

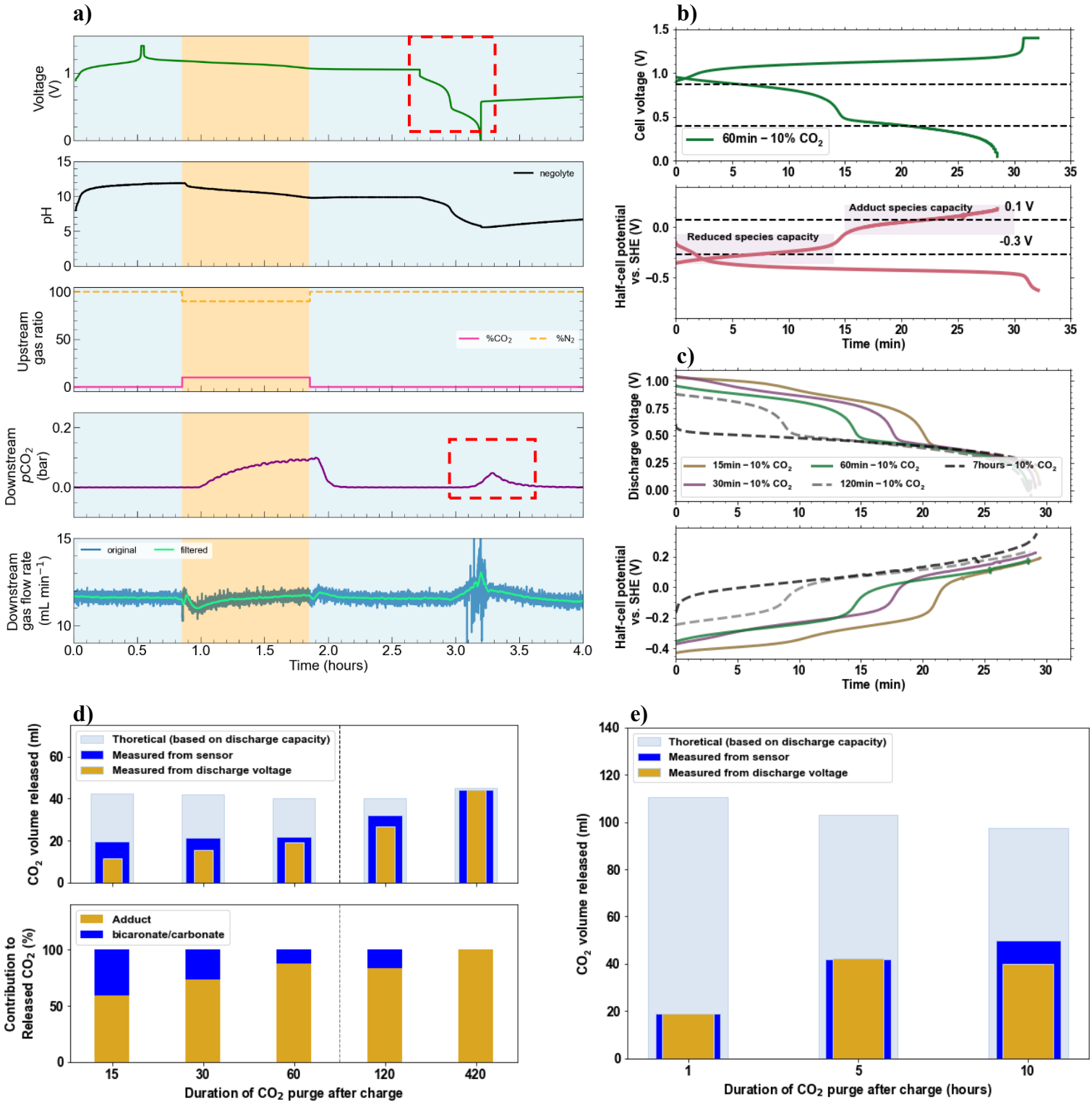

Figure 3 *a) Voltage, pH, upstream gas ratio, measured partial pressure of CO_2, and flow rate at the downstream measured during the experiment utilizing a flow cell comprising 12 ml of 0.1 M 1,5BTMAPAQ paired with 40 ml of 0.2 M BTMAPFC. The cell was charged in a nitrogen environment, followed by a controlled purge with 0.1 bar CO_2 and 0.9 bar N_2 for 60 minutes followed by a switch back to the nitrogen*

environment. b) (Top) Zoomed in full-cell voltage of the battery shown in Figure 3a, and (bottom) negative half-cell potential measured via in situ reference electrode during operation. c) Full-cell and negative half-cell potentials of the cell operated under different duration of CO_2 purge time. The solid lines depict experiments where the charge itself was conducted under N_2, whereas for the dashed line experiments, the CO_2 purging is conducted from the beginning of the charge phase. d) (Top) CO_2 release volume calculated from the CO_2 sensor measurements and the oxidation voltage signature of the adduct. For comparison, the maximum theoretical CO_2 release volume calculated from the total discharge capacity is also shown. (Bottom) the percentage contribution of each mechanism to the total capture amount. e) CO_2 release volume calculated from the CO_2 sensor measurements and the oxidation voltage signature of the adduct for 7 ml of 0.4 M of 1,4-BTMAPAQ and very diluted CO_2 concentrations of 0.01bar (1% CO2, 99% N2) under different rest durations.

In Situ Method 2: Fluorescence Microscopy-Based Visualization

We first investigate the real-time absorbance of the 1,5-BTMAPAQ species by integrating an *in situ* ultraviolet–visible (UV-Vis) spectrometer into the electrolyte flow path in an operating flow cell, as illustrated in Figure S15. Figure 4a presents the absorbance spectra of 5 mM 1-5,BTMAPAQ in 1 M KCl within a flow cell, operating against 20 mM BTMAPFc under a 100% N_2 stream to capture the real-time absorbance profiles during reduction of 1,5-BTMAPAQ in the absence of any 1,5-BTMAPAQ$(CO_2)_2^{2-}$ adduct. Under these conditions, five distinct peaks at wavelengths of 223 nm, 251 nm, and 391 nm, 487 nm and 523 nm are evident. During charging, the 223 nm peak decreases in absorbance, and the 251 nm and 391 nm peaks increase, with a new peak emerging at 430 nm, corresponding to the conversion of the molecule from its oxidized form to the reduced form. Subsequently, the battery was brought to rest, and UV-Vis spectra were monitored as a 50% CO_2/50% N_2 stream is introduced to form the adduct (Figure 4b). This methodology enabled the acquisition of spectra for both the reduced 1,5-BTMAPAQ and the 1,5-BTMAPAQ$(CO_2)_2^{2-}$ adduct species within the same experiment. Comparing the spectra at t = 0 and after half an hour of CO_2 purging, we observed minor absorbance changes, particularly at 251 nm, 391 nm and 487 nm, indicating a similarity between the spectra of the reduced species and the adduct, which poses a challenge for precise quantification of the species using this method. The full operation of the battery, involving charge and discharge cycles, was also conducted separately under N_2 and CO_2 environments in separate experiments, as illustrated in Figure S16. These experiments similarly revealed minor changes between the spectra under these conditions. Consequently, we shifted our focus to fluorescence spectroscopy to explore the potential of utilizing emission profiles as a means of differentiation.

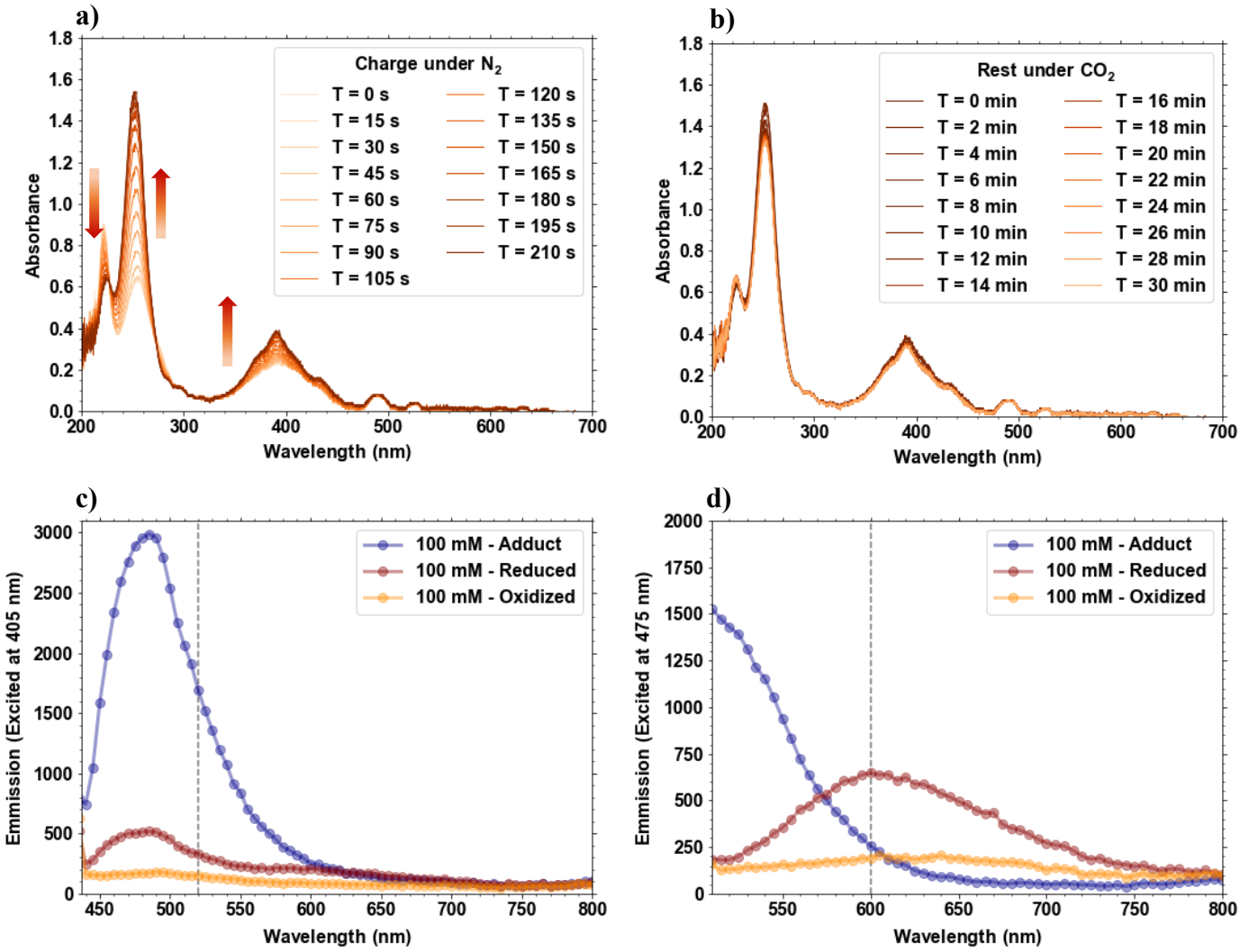

Figure 4 *a) In Situ absorbance spectra of 5 mM 1,5-BTMAPAQ dissolved in 1 M KCl during the charging phase (reduction of BTMAPAQ) in a battery operating versus 40 mM BTMAPFc (bis((3 trimethylammonio)propyl)ferrocene dichloride) in 1 M KCl under pure nitrogen phase. The absorbance spectra were taken until the charge was complete. b) In Situ absorbance spectra of 5 mM 1,5-BTMAPAQ dissolved in 1 M KCl taken during the rest time immediately after the charging phase. In the first minute,* 50% CO_2/50% N_2 *was introduced to the solution. c) Ex situ fluorescence spectra of 100 mM of the adduct, reduced and oxidized species of 1,5-BTMAPAQ excited at 405 nm. d) Ex-situ fluorescence spectra of 100 mM of the adduct, reduced and oxidized species of 1,5-BTMAPAQ excited at 475 nm.*

Figures 4c and 4d present the emission spectra of the oxidized, reduced, and adduct species of 1,5-BTMAPAQ, obtained *ex situ* using a fluorescent plate reader. The oxidized species underwent reduction in a flow battery against BTMAPFc within a glovebox, and the BTMAPAQ$(CO_2)_2^{2-}$ adduct was prepared by introducing excess dry ice to the reduced solution inside the glovebox. Subsequently, the reduced, oxidized, and adduct forms of 1,5-BTMAPAQ were sealed in a transparent well plate and transferred to the plate reader (experimental details in SI Section 4.3). Figures 4c and 4d illustrate the emission spectra of species excited at 405 nm and 475 nm, respectively. In both cases, the oxidized species shows almost

no fluorescence, whereas interestingly, both the reduced and the adduct species exhibit fluorescence, with the adduct form displaying significantly higher intensity. This intriguing trend doesn't appear to be unique to our molecule. We observed a similarly high fluorescence intensity in the adduct for other anthraquinones, including 2,2′-((9,10-dioxo-9,10-dihydroanthracene-2,6-diyl)bis(oxy))-dipropionic acid (2,6-D2PEAQ [16]) and 2-2-propionate ether anthraquinone (22PEAQ [25]), as demonstrated in Figure S17. Note that the solutions contain mixtures of different forms of the anthraquinone, for example the reduced solution contains the collection of AQ^{2-} as well as $AQH^{-}$and AQH_2. This mixture may induce diverse energy transition states, influencing the emission intensity in response to varying excitation wavelengths. However, the noteworthy insight gathered from these figures is that, through a careful selection of emission wavelength regions, we can identify areas where the fluorescence signatures of the reduced, oxidized, and adduct species of 1,5-BTMAPAQ are distinct enough to potentially enable quantification of the BTMAPAQ$(CO_2)_2^{2-}$ by careful selection of band-pass filters. Specifically, when considering an emission wavelength close to 520 nm for compounds excited at 405 nm (Figure 4c), we observe that the adduct form still exhibits high fluorescence, while the reduced species approaches the bottom of its emission peak. Conversely, selecting an emission wavelength near 600 nm for compounds excited at 475 nm (Figure 4d), we observe that the reduced form is at its peak intensity, while the adduct is at the bottom of the emission peak, displaying almost no fluorescence. Furthermore, the emission spectra of the pure bicarbonate/carbonate solutions do not show any fluorescence properties that differ from the background pH 14 solution, as depicted in Figure S18. This analysis based on the *ex situ* data suggests the possibility of leveraging the fluorescence signatures of these compounds for a dynamic, precise, and real-time exploration of the nucleophilicity-swing mechanism by monitoring the BTMAPAQ$(CO_2)_2^{2-}$ adduct concentration evolution during operation in isolation from the pH-swing mechanism.

To facilitate *in situ* tests using fluorescence signatures as a quantification method for the species, we proceeded by developing a custom-designed optically transparent microfluidic electrochemical flow cell inspired from microfluidic chips that can be integrated into a fluorescence microscope and is compatible with optical imaging, as shown in Figure 5a. The cell connects to a potentiostat for electrochemical control and acquisition and is designed with inlets/outlets for electrolyte flow into external reservoir. The cell structure includes an anion exchange membrane (DSV-N) sandwiched between two 5 by 10 mm Avcarb190 porous carbon electrodes layered in pocket molded within Polydimethylsiloxane (PDMS) half cells and two acrylic end plates for compression. The half-cell has a thickness of 8 mm, suitable for direct observation with a 10x/0.3NA Leica objective (556503) with a working distance of 11 mm mounted on a confocal microscope (Leica DMi8 body with Andor dragonfly spinning disk). The unprecedented resulting transverse resolution for local electrochemical characterization in porous electrode with this objective was 1 μm per pixel and about $25\mu m$ for the depth of field. Peristaltic pumps were employed for circulating the electrolyte, and the headspace on the negolyte side could be switched from N_2 to CO_2 during the experiments. Figure 5b displays the Widefield image of the porous electrode extracted from this cell, while Figure 5c provides a schematic representation of the experimental setup (further details can be found in SI section 4.3, Figures S19 and S20).

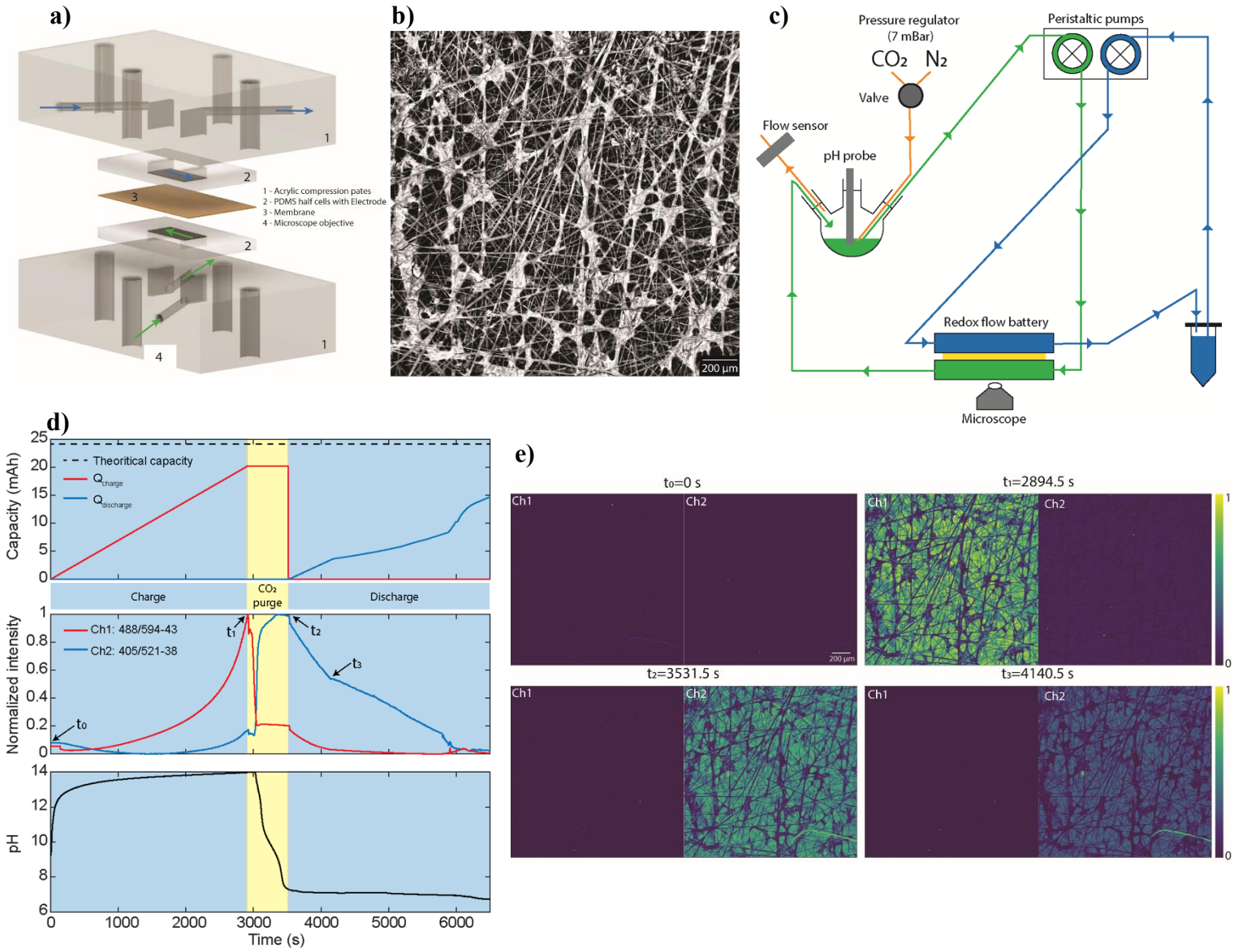

Figure 5 *a) Schematic of the custom-designed optically transparent microfluidic inspired flow cell designed for the in situ electrochemical investigation. b) Widefield optical microscopy image of the porous carbon paper electrode inside the electrochemical cell. c) Experimental setup for the study of the electrochemical carbon capture flow cells using in situ fluorescence microscopy. d) Capacity, average over an entire image normalized intensity (normalized based on the initial intensity), and pH during the operation of the microfluidic cell containing 4 ml of 0.1 M 1,5 BTMAPAQ in 1 M KCl paired with 20 ml of 0.2 M BTMAPFc in 1 M KCl under the fluorescence microscope. e) Normalized intensity at a pixel level (1 µm) of the two channels at times of interest (t_0, t_1, t_2, and t_3) shown with arrows in Figure 5d (in the normalized intensity subplot).*

To investigate the potential correlation between fluorescence intensity at wavelengths identified by the *ex situ* study and the adduct concentration, we designed an experiment wherein the battery is initially charged under N_2, followed by the introduction of CO_2. Figures 5d and 5e present the data associated with the

operation of the described microfluidic cell under the fluorescent microscope, where two channels with different excitation/absorption settings were established for monitoring. In alignment with our *ex situ* data, channel 1 was configured with an excitation wavelength of 488 nm and an emission wavelength peaking at 594 nm, corresponding to the reduced form of 1,5-BTMAPAQ. Meanwhile, channel 2 was set up with an excitation wavelength of 405 nm and an emission wavelength peaking at 521 nm, corresponding to the adduct form of 1,5-BTMAPAQ. At the initial time point (t_0=0), no fluorescence is evident, consistent with the ex-situ data, attributed to the oxidized compound not fluorescing within the chosen wavelengths. As the charging process begins and progresses under a nitrogen atmosphere, the reduced form becomes fluorescent (channel 1, t_1 = 2894.5 s), with intensity increasing alongside the charging capacity. During this period, there is a minor change in the fluorescence intensity of channel 2, as expected due to the absence of any adduct species. Note that the pH of the solution swings up, given that the reaction is proton-coupled. At the end of the charge, the nitrogen headspace is switched to 1 bar CO_2 to initiate the carbon capture process. Subsequent purging of CO_2 induces the conversion of the reduced form to the CO_2-quinone adduct, resulting in the loss of fluorescence in channel 1. Intriguingly, channel 2, characterized by a distinct fluorescence signal from the adduct, becomes intense. Note that as the carbon dioxide is purged, the pH drops to 7 because the hydroxides are being utilized for bicarbonate/carbonate formation in parallel with the adduct formation. Upon discharging, the fluorescence gradually fades (t_3 = 4140.5). During the discharging phase, we intentionally altered the discharge current rate to demonstrate the correlation between the intensity change and the rate of discharge, as evidenced by the comparison between Figure 5c1 and 5c2. CO_2 gas bubbles formed as a result of the CO_2 release during discharge are also evident (see Video S1), more clearly observed near the outlet of the cell where bubble accumulation occurs.

While the intensity appears to correlate with the concentration of the adduct, for this method to be applicable for quantification we must calibrate the measurement, i.e. establish a correlation between intensity and concentration under a known condition. The most rigorous approach is either to inject a known concentration of the isolated solution of adduct into the cell and measure the emission intensity or to upgrade the setup with a downstream CO_2 sensor and flow meter and a reference electrode. This allows for measuring the potential of the negative half-cell against a reference under a known condition, creating a standard concentration-intensity calibration plot. In this proof of concept, we make an assumption that operating the microfluidic cell under a pure stream of CO_2 (1 bar) from the beginning of the charging process facilitates adduct formation and results in the full dominance of BTMAPAQ$(CO_2)_2^{2-}$ adduct, consistent with our thermodynamic view. Under such an assumption, the fully charged capacity of 37 C measured by the potentiostat is attributed to the production of the adduct, which can be correlated with the 6000 units of intensity measured by the microscope in channel 2. Utilizing this established calibration, we then conducted an experiment involving a charging phase under a pure nitrogen stream, followed by purging the system with a pure stream of CO_2 to capture carbon dioxide for only a short wait time afterwards. It is anticipated that the resulting intensity of the adduct, and hence the concentration, would be lower than observed in the first case (Figure 6a). Indeed, the concentration of the adduct formed under these conditions, extracted from the intensity of channel 2, is measured at 0.035 M, representing approximately 70% of the total capacity. The method is equally applicable for the detection of adducts under dilute streams of CO_2. Figure 6c illustrates the data extracted from the operation of the microfluidic cell under dilute streams of 1% and 400 ppm (100% included for comparison). We observe the formation of 0.025 M of the adduct under the dilute condition of 0.01 bar CO_2 (1% CO_2, 99% N_2) within 50 minutes, detected in real-time during the formation. This short timeframe (50 minutes) appears insufficient for any adduct to form under the 400 ppm condition. Moreover, the method is robust enough to be employed for

the extraction of kinetic rates of adduct formation chemical reactions. To achieve this, we increased the imaging rate to sub-second intervals (125 ms) and conducted experiments using 1,5BTMAPAQ and 1,8BTMAPAQ isomers. Through CV analysis, we demonstrated a kinetic rate constant for the 1,5BTMAPAQ isomer almost three times that of the 1,8BTMAPAQ isomer (Table 1). The *in situ* fast imaging of the adduct formation for the two isomers similarly reveals a threefold difference in kinetic rates.

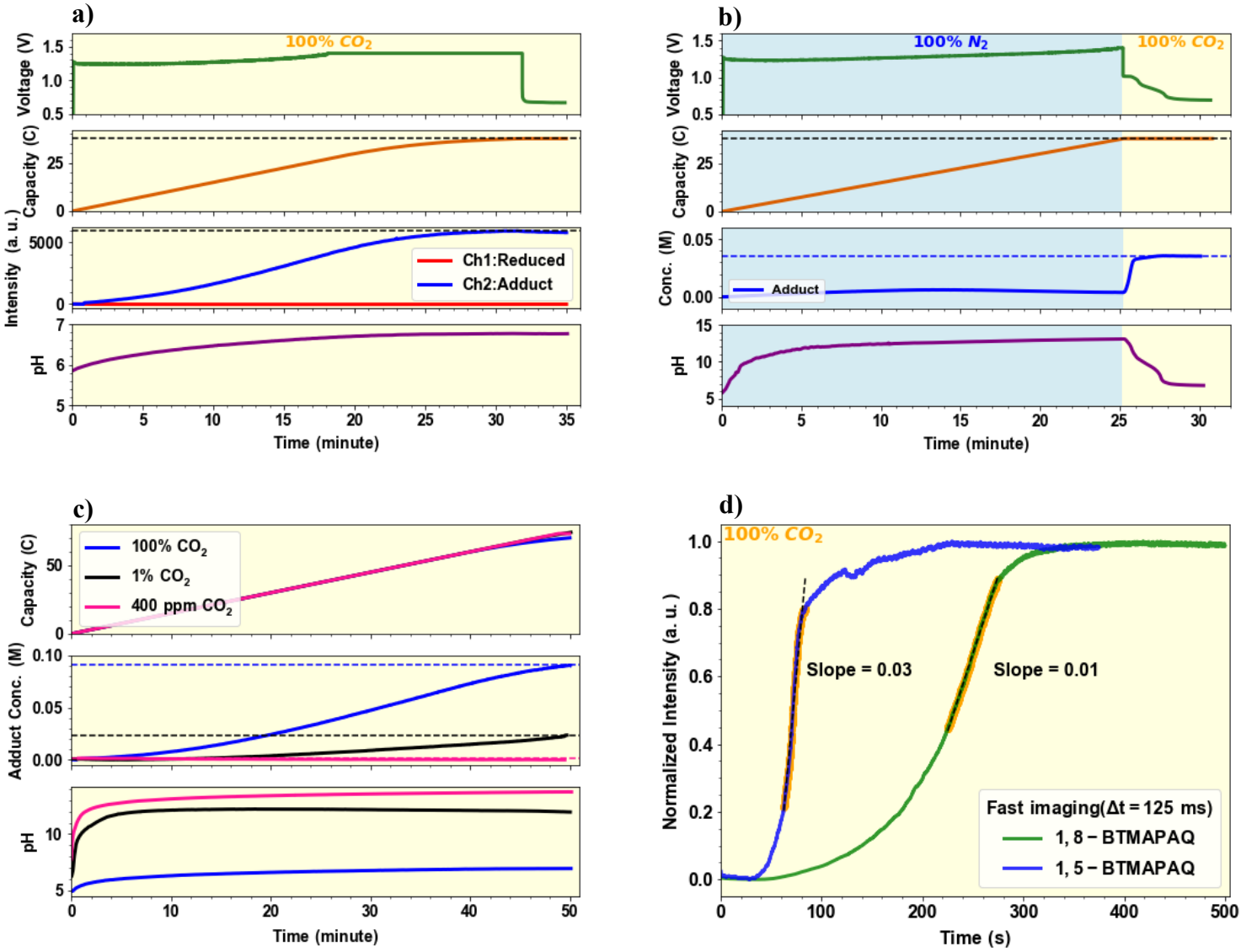

Figure 6 *Information extracted from the operation of the microfluidic flow cell under the fluorescence microscope under nitrogen and carbon dioxide streams, monitoring channels with excitation and absorption wavelengths 488/594, respectively in channel 1 and 405/521, respectively for channel 2. Channel 1 wavelengths correspond to the reduced form concentration and channel 2 correspond to the adduct concentration. a) Voltage, capacity, in situ fluorescence intensity and pH of a solution of 5 mM 1,5-BTMAPAQ dissolved in 1 M KCl under pure stream of CO_2. b) Voltage, capacity, concentration (extracted*

from in situ fluorescence intensity) and pH of a solution of 5 mM 1,5-BTMAPAQ dissolved in 1 M KCl under pure stream of CO_2. c) Capacity, adduct concentration and pH at three different CO_2 partial pressures mixed with nitrogen. d) Normalized intensity of adduct versus time measured with increased imaging rate to sub-second intervals (125 ms) for two isomers of 1,5BTMAPAQ and 1,8BTMAPAQ.

The results presented herein serve as proof-of-concept for the capabilities of *in situ* fluorescence microscopy in studying quinone-based carbon capture systems. To fully harness the potential of this method, incorporating CO_2 sensors and flowmeters into the negolyte reservoir's path is crucial. This integration would enable a direct comparison between the adduct concentration measured by the fluorescence microscope and the total captured capacity measured by the CO_2 sensor and the flow meter. Moreover, establishing a rigorous correlation between intensity and concentration is crucial for enhancing the reliability and accuracy of quantification processes. Additionally, due to the partial stability of the species in the oxygen environment and the open-air configuration of our microscope, experiments had to be limited to less than an hour. As the field advances in designing more stable compounds in oxygen environments, experiments can be conducted without interference from oxygen over longer durations. Alternatively, an experimental setup with more suitable sealing can be devised. Lastly, the integration of mass flow controllers would enhance systematic control over the ratio of CO_2 to nitrogen in the headspace of the negolyte reservoir, enabling a more methodical and comprehensive study. The method provides the capability to distinguish between the oxidized, reduced, and adduct species and quantify their relative concentration with sub-second time resolution through their fluorescence signatures at single digit micrometer resolution, demonstrating a highly promising technique for studying such systems. Furthermore, the method of conducting parallel monitoring of the fluorescence signature of the species involved in a reaction is inspiring for studying reaction mechanisms and concentration quantification in other systems.

Summary

In the present work, we began by providing a thermodynamic overview of the interplay between nucleophilicity-swing and pH-swing mechanisms as functions of the properties of a hypothetical quinone molecule. We then proceeded to focus on the kinetic and thermodynamic properties of the BTMAPAQ isomers, revealing a strong thermodynamic tendency for BTMAPAQ to form an CO_2-adduct, though kinetically, this mechanism is predicted to be slower than the pH-swing mechanism. We then proceeded to introduce two new techniques for the experimental differentiation between the contributions of the pH-swing mechanism and nucleophilicity-swing mechanism. The first method was based on the voltage signature difference between the reduced and the adduct form of the quinone, conducted by incorporating an *in situ* reference electrode and calculating the adduct formation from the capacity delivered at the voltage signature of the quinone-adduct compound. In the second method, we introduced a non-invasive, *in situ* approach using fluorescence microscopy, providing the unique capability to isolate the contribution of the nucleophilicity mechanism through quinone-adduct quantification. This powerful technique holds significant promise for studying similar systems in detail, demonstrating a new method for investigation of carbon capture processes.

Acknowledgment

This research was supported by the National Science Foundation through grant CBET-1914543 and by U.S. DOE award DE-AC05-76RL01830 through PNNL subcontract 535264. K.A. was supported in part through the Natural Sciences and Engineering Research Council of Canada (NSERC)

Postdoctoral Fellowship (PDF) program [application number PDF-557232-2021]. The authors also thank Eric Fell, Thomas George, Kyumin Lee, and Dr. Martin Jin for valuable discussions.

References

[1]M.Y. Suberu, M.W. Mustafa, and N. Bashir, "Energy Storage Systems for Renewable Energy Power Sector Integration and Mitigation of Intermittency", *Renewable and Sustainable Energy Reviews* **35**, 499 (2014). https://doi.org/https://doi.org/10.1016/j.rser.2014.04.009

[2]M. Bui, C.S. Adjiman, A. Bardow, E.J. Anthony, A. Boston, S. Brown, P.S. Fennell, S. Fuss, A. Galindo, L.A. Hackett, J.P. Hallett, H.J. Herzog, G. Jackson, J. Kemper, S. Krevor, G.C. Maitland, M. Matuszewski, I.S. Metcalfe, C. Petit, G. Puxty, J. Reimer, D.M. Reiner, E.S. Rubin, S.A. Scott, N. Shah, B. Smit, J.P.M. Trusler, P. Webley, J. Wilcox, and N. Mac Dowell, "Carbon Capture and Storage (Ccs): The Way Forward", *Energy & Environmental Science* **11**, 1062 (2018). https://doi.org/10.1039/c7ee02342a

[3]G.T. Rochelle, "Amine Scrubbing for CO_2 Capture", *Science* **325**, (2009).

[4]G.T. Rochelle, "Thermal Degradation of Amines for CO_2 Capture", *Current Opinion in Chemical Engineering* **1**, 183 (2012). https://doi.org/10.1016/j.coche.2012.02.004

[5]K.M. Diederichsen, R. Sharifian, J.S. Kang, Y. Liu, S. Kim, B.M. Gallant, D. Vermaas, and T.A. Hatton, "Electrochemical Methods for Carbon Dioxide Separations", *Nature Reviews Methods Primers* **2**, (2022). https://doi.org/10.1038/s43586-022-00148-0

[6]Y. Liu, H.Z. Ye, K.M. Diederichsen, T. Van Voorhis, and T.A. Hatton, "Electrochemically Mediated Carbon Dioxide Separation with Quinone Chemistry in Salt-Concentrated Aqueous Media", *Nat Commun* **11**, 2278 (2020). https://doi.org/10.1038/s41467-020-16150-7

[7]X. Li, X. Zhao, Y. Liu, T.A. Hatton, and Y. Liu, "Redox-Tunable Lewis Bases for Electrochemical Carbon Dioxide Capture", *Nature Energy* **7**, 1065 (2022). https://doi.org/10.1038/s41560-022-01137-z

[8]S. Jin, M. Wu, R.G. Gordon, M.J. Aziz, and D.G. Kwabi, "pH Swing Cycle for CO_2 Capture Electrochemically Driven through Proton-Coupled Electron Transfer", *Energy & Environmental Science* **13**, 3706 (2020). https://doi.org/10.1039/d0ee01834a

[9]S. Jin, M. Wu, Y. Jing, R.G. Gordon, and M.J. Aziz, "Low Energy Carbon Capture Via Electrochemically Induced Ph Swing with Electrochemical Rebalancing", *Nature communications* **13**, 1 (2022). https://doi.org/https://doi.org/10.1038/s41467-022-29791

[10]B. Gurkan, F. Simeon, and T.A. Hatton, "Quinone Reduction in Ionic Liquids for Electrochemical CO_2 Separation", *ACS Sustainable Chemistry & Engineering* **3**, 1394 (2015). https://doi.org/10.1021/acssuschemeng.5b00116

[11]K.M. Diederichsen, Y. Liu, N. Ozbek, H. Seo, and T.A. Hatton, "Toward Solvent-Free Continuous-Flow Electrochemically Mediated Carbon Capture with High-Concentration Liquid Quinone Chemistry", *Joule* **6**, 221 (2022). https://doi.org/10.1016/j.joule.2021.12.001

[12]J.M. Barlow and J.Y. Yang, "Oxygen-Stable Electrochemical CO_2 Capture and Concentration with Quinones Using Alcohol Additives", *J Am Chem Soc* **144**, 14161 (2022). https://doi.org/10.1021/jacs.2c04044

[13]S. Voskian and T.A. Hatton, "Faradaic Electro-Swing Reactive Adsorption for CO_2 Capture", *Energy & Environmental Science* **12**, 3530 (2019). https://doi.org/10.1039/c9ee02412c

[14]D. Wielend, D.H. Apaydin, and N.S. Sariciftci, "Anthraquinone Thin-Film Electrodes for Reversible CO_2 Capture and Release", *Journal of Materials Chemistry A* **6**, 15095 (2018). https://doi.org/10.1039/c8ta04817g

[15]Y. Jing, K. Amini, D. Xi, S. Jin, A. Alfaraidi, E. Kerr, R. Gordon, and M. Aziz, "Electrochemically Induced CO_2 Capture Enabled by Aqueous Quinone Flow Chemistry", *ChemRxiv* (2023). https://doi.org/10.26434/chemrxiv-2023-nfg6z

[16]E.F. Kerr, Z. Tang, T.Y. George, S. Jin, E.M. Fell, K. Amini, Y. Jing, M. Wu, R.G. Gordon, and M.J. Aziz, "High Energy Density Aqueous Flow Battery Utilizing Extremely Stable, Branching-Induced High-Solubility Anthraquinone near Neutral Ph", *ACS Energy Letters* **8**, 600 (2022). https://doi.org/10.1021/acsenergylett.2c01691

[17]D.G. Kwabi, Y. Ji, and M.J. Aziz, "Electrolyte Lifetime in Aqueous Organic Redox Flow Batteries: A Critical Review", *Chem Rev* **120**, 6467 (2020). https://doi.org/10.1021/acs.chemrev.9b00599

[18]M. Wu, M. Bahari, Y. Jing, K. Amini, E.M. Fell, T.Y. George, R.G. Gordon, and M.J. Aziz, "Highly Stable, Low Redox Potential Quinone for Aqueous Flow Batteries", *Batteries & Supercaps* e202200009 (2022). https://doi.org/https://doi.org/10.26434/chemrxiv-2021-rjzdn).

[19]L.N.R. Rabindra N. Roy, Kathleen M. Vogel, C. Porter-Moore, Tara Pearson, and F.J.M. Catherine E. Good, Douglas M. Campbell "The Dissociation Constants of Carbonic Acid in Seawater at Salinities 5 to 45 and Temperatures 0 to 45°C", *Marine Chemistry* **44**, 249 (1993).

[20]F. Simeon, M.C. Stern, K.M. Diederichsen, Y. Liu, H.J. Herzog, and T.A. Hatton, "Electrochemical and Molecular Assessment of Quinones as CO_2-Binding Redox Molecules for Carbon Capture", *The Journal of Physical Chemistry C* **126**, 1389 (2022). https://doi.org/10.1021/acs.jpcc.1c09415

[21]W.C. Xiaoguang Wang, Robert Burns, Nichola McCann, and Marcel Maeder, "Comprehensive Study of the Hydration and Dehydration Reactions of Carbon Dioxide Inaqueous Solution", *Journal of Physical Chemistry A* **114**, 1734 (2009).

[22]C. Costentin, "Electrochemical Approach to the Mechanistic Study of Proton-Coupled Electron Transfer", *Chem Rev* **108**, 2145 (2008). https://doi.org/10.1021/cr068065t

[23]E.W. Zhao, T. Liu, E. Jonsson, J. Lee, I. Temprano, R.B. Jethwa, A. Wang, H. Smith, J. Carretero-Gonzalez, Q. Song, and C.P. Grey, "In Situ NMR Metrology Reveals Reaction Mechanisms in Redox Flow Batteries", *Nature* **579**, 224 (2020). https://doi.org/10.1038/s41586-020-2081-7

[24]K. Amini, Y. Jing, J. Gao, J.D. Sosa, R.G. Gordon, and M.J. Aziz, "Electrochemical Performance of Mixed Redox-Active Organic Molecules in Redox Flow Batteries", *Journal of The Electrochemical Society* (2023). https://doi.org/10.1149/1945-7111/ad1295

[25]K. Amini, E.F. Kerr, T.Y. George, A.M. Alfaraidi, Y. Jing, T. Tsukamoto, R.G. Gordon, and M.J. Aziz, "An Extremely Stable, Highly Soluble Monosubstituted Anthraquinone for Aqueous Redox Flow Batteries", *Advanced Functional Materials* (2023). https://doi.org/10.1002/adfm.202211338